Shot-noise limited optical hybrid based on fused fiber couplers

KRISTEN HAGAN,[1] KEVIN C. ZHOU,[1] AL-HAFEEZ DHALLA,[1] JOSEPH A. IZATT[1, 2,*]

[1]*Department of Biomedical Engineering, Duke University, Durham, NC 27708, USA*
[2]*Department of Ophthalmology, Duke University Medical Center, Durham, NC 27710, USA*
**Corresponding author: joseph.izatt@duke.edu*

Received XX Month XXXX; revised XX Month, XXXX; accepted XX Month XXXX; posted XX Month XXXX (Doc. ID XXXXX); published XX Month XXXX

We describe a fiber-based coherent receiver topology which utilizes intrinsic phase shifts from fiber couplers to enable instantaneous quadrature projection with shot-noise limited signal-to-noise ratio (SNR). Fused 3x3 fiber couplers generate 3 phase-shifted signals simultaneously that can be combined with quadrature projection methods to detect magnitude and phase unambiguously. We present a novel differential detection topology which utilizes a combination of 3x3 and 2x2 couplers to enable quadrature projection with fully differential detection. We present a mathematical analysis of this 3x3 differential detection topology, extended methods for signal calibration, and SNR analysis. We characterize the SNR advantage of this approach and demonstrate a sample application illustrating simultaneous magnitude and phase imaging of a chrome-on-glass test chart.

Traditional optical detection yields output signals proportional to the optical field intensity due to the use of square-law detectors. For many applications, detection of the full complex field is required, for applications ranging from fiber sensors and optical metrology, to coherent lidar-based autonomous guidance systems, to phase-shift keying approaches in optical communications. For each of these and many additional applications, detection at the fundamental shot-noise limit is of maximum utility.

Interferometry provides the favored approach for coherent optical detection; however, a prerequisite for fast and accurate reconstruction of signal magnitude and phase is the reliable, optimally simultaneous generation of phase-separated optical signals, preferably in quadrature. Many coherent detection approaches utilizing interferometry have been developed [1], including sequential phase-stepped and phase-sweeping interferometry [2-4], polarization-encoded optical systems [5, 6], phase generation carrier approaches [7], and 90° optical hybrids [8] based on fixed path-length delays achievable with integrated photonics platforms. Some of these approaches have been demonstrated with differential detection which cancels excess noise sources, allowing for shot-noise limited detection. However, each of these approaches also has significant limitations, such as the need for sequential phase-stable measurements, issues with chromatic effects and/or birefringent samples, the need for significant averaging due to band-pass filtering, and the high fixed costs of integrated optical device design and manufacture, respectively. The latter limitation has restricted the availability of commercial 90° optical hybrids to telecommunications wavelengths, where they remain quite expensive.

An attractive alternative to conventional phase-separation methods in coherent interferometry is the use of low-cost fused 3x3 fiber couplers which ideally generate, for even power splitting, 3 x 120° phase-shifted signals simultaneously [9, 10]. These signals can then be projected onto the complex plane to extract unambiguous magnitude and phase data, thereby comprising a simple, cost-effective, colorless [11, 12] solution for instantaneous coherent detection [13-15]. Previous work utilizing these couplers suffered

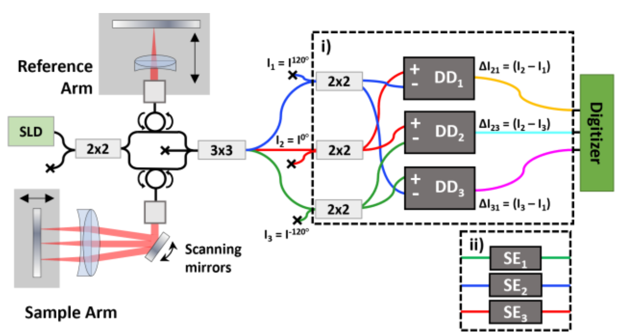

Figure 1. Schematic of coherent fiber-based system utilizing a 3x3 fiber coupler to create 3 phase-separated signals simultaneously. Inset i) highlights cascaded design using both 3x3 and 2x2 fiber couplers (FC) with 50:50 splitting ratios. The 2x2 FCs act as power-splitters and enable the use of differential detection (DD) as three unique signals (ΔI_{ij}) can be generated and then sampled by the digitizer. Inset ii) shows previous detection arm implementations using the 3x3 coupler outputs directly with single-ended (SE) detection. Unused fiber coupler ports are denoted with an 'x'.

from (1) inaccuracies of reconstructed magnitude and phase due to deviations in power splitting, phase offset, and/or phase drift in the fiber coupler from manufacturing and environmental conditions [10, 13], and (2) the use of single-ended photodetectors and thus the lack of any means for achieving shot-noise limited SNR using fully differential detection. Recent developments in coupler fabrication have improved accuracy of power splitting and stability of available 3x3 couplers, and calibration algorithms [16, 17] present the opportunity to improve the accuracy of the reconstructed magnitude and phase data by directly measuring DC offset, fringe depth amplitude, and phase offsets of each signal. However, despite these improvements, the lack of shot-noise limited detection capability has restricted applications of 3x3 coherent receivers to high-signal and/or low-noise situations.

Many 2x2 coupler-based interferometric systems incorporate balanced receivers to improve signal-to-noise ratio (SNR) by cancelling excess noise and maximizing the digitizer's dynamic range but do not allow for quadrature detection as the mutual phase offset between output signals is 180° [18]. This paper presents a simple and cost-effective approach to quadrature detection using 3x3 couplers with balanced detectors to perform hardware-based complex signal reconstruction that is less sensitive to noise as compared to an unbalanced or single-ended 3x3 detection scheme [10, 11, 13, 16, 19, 20]. This system has the potential to push the limits of coherent detection speed and instantaneous phase imaging, especially in high-speed or high-performance applications such as coherent lidar and optical communications.

Figure 1 illustrates the design of the proposed coherent receiver which benefits from all the advantages provided by balanced detection while generating instantaneous complex-valued data using the 3x3 coupler. Light from a 1560 ± 30 nm superluminescent diode (Inphenix, IPSDD1502C) is split via a 75:25 2x2 coupler into matching circulator ports (Agiltron, OCPI-1550) in the reference and sample arms. For an example 2D phase imaging application, the sample arm incorporates a telecentric confocal scanning geometry on a sample object under test using galvanometer mirrors (ScannerMax, Compact506). The sample and imaging lens pair is mounted to a translation stage to allow for focus adjustment and the ability to maintain telecentricity. The reference arm is a simple reflective design where the planar mirror is translated to adjust the ~18 µm coherence gate which helps to mitigate artifacts from spurious reflections from optical system elements. Light returning from both arms is routed from their respective circulators into the 3x3 coupler (Phoenix Photonics, MFC-3-1550) which generates 3 phase-shifted signals (Fig. 2a). These are fed directly into 3 50:50 2x2 fiber couplers (Thorlabs, TN1550R5A2) which create 2 copies of each interferometric signal (Fig. 1). These copies are then used to perform hardware-based subtraction via differential detection which 1) mitigates common-mode noise, 2) maximizes dynamic range of the detector, 3) increases amplitude of resultant signals, and 4) performs subtraction needed based on theoretical equations for complex signal reconstruction.

The phase-shifted signal outputs from the 3x3 fused fiber couplers have the general form of $I_i = A_i + B_i \cos\,(2k_0\Delta z + \delta_i)$ where i=1,2,3 and A_i is the DC value dependent on the sample and reference arm reflectivity values and the power of the returned light, B_i is the fringe depth of the interferogram, $k_o = 2\pi/\lambda_o$ is the wavenumber of the light at wavelength λ_o, Δz is the difference in optical path length between reference and sample arms, and δ_i is the phase offset generated by the coupler. An ideal 3x3 coupler with

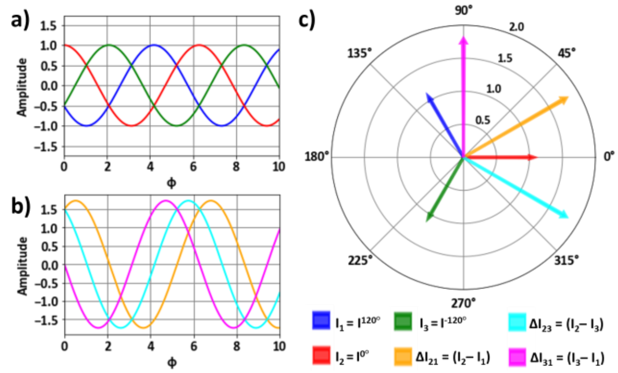

Figure 2. Signal simulation through an ideal 3x3 system assuming each real I_x signal has equal DC offsets, equal AC fringe depth. (a) Direct outputs of a 3x3 coupler with inherent 120° phase shifts. (b) Differential signal outputs (ΔI_{ij}) from DD topology which have $\sqrt{3}$x improvement in signal amplitude. (c) Phasor diagram shows the phase and amplitude differences between the six signals. A scaled average of ΔI_{21} and ΔI_{23} generates a phasor with zero angle (real), while ΔI_{31} generates a purely imaginary phasor.

an equal power splitting ratio generates three signals (i=1, 2, 3) with δ = 120° offsets (Fig. 2a) that can be combined to reconstruct the complex signal as in sequential phase-stepping interferometry [2, 9, 10] :

$$Re(I_0) = B\cos(2k_0\Delta z) = \frac{2I_2-(I_1+I_3)}{3} = \frac{\Delta I_{21}+\Delta I_{23}}{3}, \quad \textbf{(1)}$$

$$Im(I_0) = B\sin(2k_0\Delta z) = \frac{(I_3-I_1)}{\sqrt{3}} = \frac{\Delta I_{31}}{\sqrt{3}}, \quad \textbf{(2)}$$

where $\Delta I_{ij} = I_i - I_j$. The idea for differential detection stems from the observation that the real and imaginary parts in Eqs. (1-2) contain all three combinatorially possible differences between the 3x3 fused fiber outputs I_1, I_2, I_3, thus presenting the opportunity for symmetric differential detection. In fact, the differential signals ΔI_{21}, ΔI_{23}, ΔI_{31} have the same form as the original output signals I_1, I_2, I_3 but have been amplified by $\sqrt{3}$x and have relative phase shifts of -30°, 30° and 90° between them in the ideal case (Fig. 2b-c). Graphically, adding the +/-30° vectors corresponding to ($\Delta I_{21}+\Delta I_{23}$) in Eq. (1) generates the real component on the 0° axis, in quadrature with the imaginary component on the 90° axis corresponding to ΔI_{31} in Eq. (2). Thus, subtraction in the differential detectors not only removes both DC contributions and excess noise, but also directly creates scaled versions of Eqs. (1-2) directly.

In reality, these differential signals, ΔI_{21}, ΔI_{23}, ΔI_{31}, are affected by unbalanced DC and AC offsets as well as phase shift deviations. They can be written in a general extended format to include the cascaded error from actual system parameters ($A_{ij}, B_{ij}, \delta_{ij}$):

$$\Delta I_{ij} = A_{ij} + B_{ij}\cos(2k_0\Delta z - \delta_{ij}), \quad \textbf{(3)}$$

$$A_{ij} = A_i - A_j, \quad \textbf{(4)}$$

$$B_{ij} = \sqrt{(B_j\sin\delta_j - B_i\sin\delta_i)^2 + (B_i\cos\delta_i - B_j\cos\delta_j)^2}, \quad \textbf{(5)}$$

$$\delta_{ij} = \tan^{-1}\left(\frac{B_j\sin\delta_j - B_i\sin\delta_i}{B_i\cos\delta_i - B_j\cos\delta_j}\right), \quad \textbf{(6)}$$

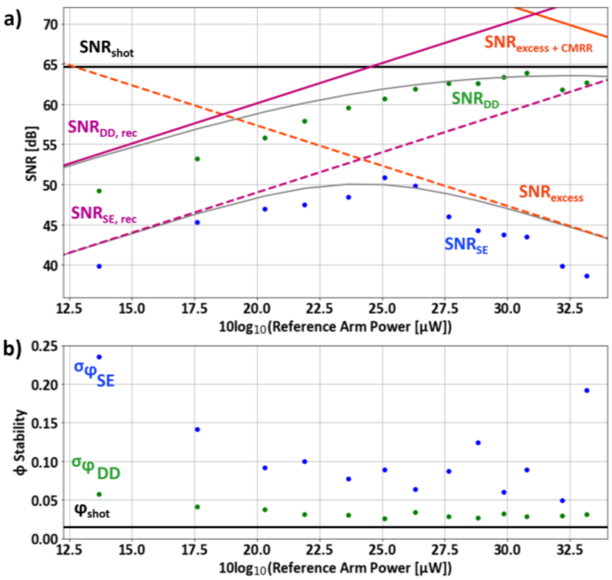

Figure 3. (a) SNR comparison between DD and SE detection topologies as a function of reference arm power. Experimental SNR values are plotted as scatter points. Theoretical shot-noise-limited (SNR_{shot}), receiver-noise-limited (SNR_{rec}), and excess-noise-limited (SNR_{excess}) values are plotted for reference using definitions from [6]. Gray lines indicate SNR for both topologies summing all noise contributions. The improvement in SNR in the DD scheme based on ~25 dB CMRR specified by the DD manufacturer is included in the SNR_{excess} plotted. (b) Phase stability calculated as standard deviation of phase reconstruction is shown.

Given ideal conditions, these equations reduce to the form found in Fig. 2b-c. We can perform calibration directly on the differential outputs via ellipse-fitting methods described in [16], and rearrange the simplified Eqs. (3-6) to formulate a matrix equation which uses ΔI_{21} as a reference that ΔI_{23} and ΔI_{31} are phase-shifted relative to:

$$\begin{bmatrix} \Delta I_{21} - A_{21} \\ \Delta I_{23} - A_{23} \\ \Delta I_{31} - A_{31} \end{bmatrix} = \begin{bmatrix} B_{21} & 0 \\ B_{23} \cos \delta_{23} & B_{23} \sin \delta_{23} \\ B_{31} \cos \delta_{31} & -B_{31} \sin \delta_{31} \end{bmatrix} \begin{bmatrix} Re \\ Im \end{bmatrix}. \quad \textbf{(7)}$$

The least-squares solution to the matrix solves for the real ($\cos 2k_0\Delta z$) and imaginary parts ($\sin 2k_0\Delta z$) of the desired complex-valued signal, from which the magnitude, |B|, and phase, φ, can be calculated.

To evaluate the system performance, we collected SNR measurements for the two topologies presented in Fig. 1 at various reference arm powers. We generated excess noise in the source by connecting a 150kHz, 0.25 mV_{pp} noise signal from a digital oscilloscope/function generator (Digilent, ADP3450) into the modulation port on the source's current controller (Thorlabs, LDC205C). For the differential case, we used 3 balanced receivers (Thorlabs, PDB450C) set to 4 MHz bandwidth with 10^5 V/A gain. For the single-ended topology, we used 3 photodetectors (Koheron, PD10S) with 50 kV/A gain and up to 50 MHz bandwidth. This photodetector was selected as its noise equivalent power of 2 pW/√Hz was similar to the 1.55 pW/√Hz specification for the balanced receivers. Also, the single detectors could tolerate input power up to 1.3 mW which was needed for measuring SNR at various reference arm power levels. The digital oscilloscope sampled and digitized the three signals at 10 MHz.

Neutral density filters were placed in the sample arm to attenuate the signal (> 25 dB), and the reference arm's path length was adjusted to be within a coherence length of the sample arm. At each reference power, data was taken with and without the sample arm blocked. Experimental SNR was calculated by taking the mean of the reconstructed magnitude over 1 ms, divided by the standard deviation of the noise signal taken with the sample arm blocked. Results from both topologies as well as theoretical SNR values are plotted in Fig. 3(a). In Fig. 3(b), the measured phase stability is also plotted.

We derived the theoretical shot-noise limited SNR for our differential detection scheme by first considering the signal outputs from the 3x3 couplers in relation to the powers in both the reference and sample arms:

$$I_i = \frac{\rho}{3}\left(P_r + P_s + 2\sqrt{P_r P_s}\cos(2k_0\Delta z + \delta_i)\right), \quad \textbf{(8)}$$

where P_r is the power from the reference arm multiplied by the system transmission, P_s is the power from the sample arm multiplied by the system transmission, ρ is the responsivity of the InGaAs detectors, and δ_i is -120°, 0, and 120°. The factor of three included here is based on the equal power split in the 3x3 coupler. The 2x2 couplers then create 2 copies of each I_i (denoted with prime notation) which are scaled by ½ from equal power splitting. The squared magnitude is then calculated as:

$$|B|^2 = \left(\frac{\frac{I_2}{2} + \frac{I_{2'}}{2} - \left(\frac{I_1}{2} + \frac{I_3}{2}\right)}{3}\right)^2 + \left(\frac{\frac{I_{3'}}{2} + \frac{I_{1'}}{2}}{\sqrt{3}}\right)^2 = \frac{\rho^2 P_r P_s}{9}, \quad \textbf{(9)}$$

where signals expressed in Eq. (9) are substituted into Eqs. (1-2) to generate the real and imaginary components. The photocurrent variance due to shot-noise at each single photodetector (6 in total) is defined as $\sigma^2_{shot} = 2qW\langle\frac{I_i}{2}\rangle$ [21] where W is detection bandwidth and q is electronic charge. The total variance is calculated using error propagation:

$$\sigma^2_{|B|} = \left(\frac{\partial|B|}{\partial I_1} + \frac{\partial|B|}{\partial I_{1'}} + \frac{\partial|B|}{\partial I_2} + \frac{\partial|B|}{\partial I_{2'}} + \frac{\partial|B|}{\partial I_3} + \frac{\partial|B|}{\partial I_{3'}}\right)\sigma^2_{shot} = \frac{5qW\rho P_r}{27}, \quad \textbf{(10)}$$

assuming $P_r >> P_s$. Finally, the shot-noise limited SNR is determined as:

$$SNR_{shot} = \frac{|B|^2}{\sigma^2_{|B|}} = \frac{3\rho P_s}{5qW}, \quad \textbf{(11)}$$

which suggests that the differential 3x3 case has ideal SNR between the single-ended and differential 2x2 interferometer cases [21]. This appears reasonable, since the noise variance for the 3x3 differential system increases due to multiple independent receivers, while the 120° out-of-phase subtractions generate a $\sqrt{3}$x signal gain (as opposed to the 2x improvement when subtracting 180° out-of-phase signals).

As seen in Fig. 3, in all cases the data matches the theory quite well, demonstrating >20dB SNR improvement at high power with near shot-noise limited performance throughout. the presence of substantial excess noise due to the rejection of this common-mode signal. The single-ended topology becomes particularly troublesome at high reference arm powers due to uncancelled excess noise. Additionally, we plot the measured standard deviation in reconstructed phase values for both detection schemes against the theoretical phase sensitivity limit [22]. The differential scheme more closely approaches the theoretical value where sufficient reference power allows shot-noise limited performance. Thus, we surmise that both excess and receiver noise contributed to phase instability of previous single-ended designs.

One potential application of this coherent detection method is in phase imaging. We introduced a telecentric scanner (Fig. 1) in the sample arm to demonstrate the capability to resolve phase information in a high-noise environment (150kHz, 0.25 mV_{pp} noise signal). We wrote custom real-time control and acquisition software using the Vortex library which controlled the XY galvanometer scanners and acquired 3 signals for reconstruction of magnitude and phase [23]. A 1951 USAF target (Thorlabs, R1DS1P) was imaged using a 40kHz sampling rate (NI USB 6341) with 250 uW incident on the sample and 500 uW on the reference arm.

Magnitude and phase data were extracted via Eq. (7) using calibration parameters measured prior to imaging. The magnitude images were normalized based on their different gain values. Figure 4 shows imaging results for both detection schemes. Though both schemes average to the same result, the differential scheme has

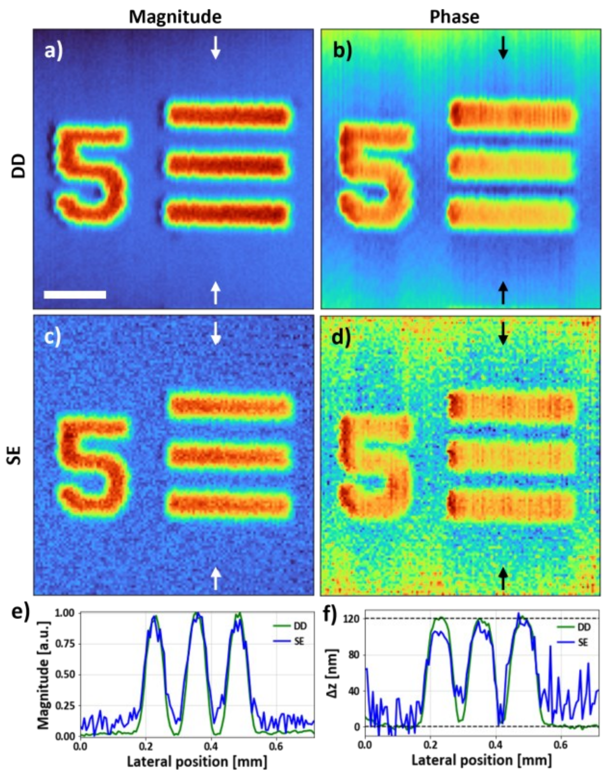

Figure 4. Example application and comparison of simultaneous magnitude and phase imaging of 120 nm tall chrome features on standard USAF test chart (Group 2 Element 5) in the presence of additive noise. (a) Magnitude and (b) phase image taken using the using the differential detection (DD) topology. (c) Magnitude and (d) phase image taken using the using the single-ended (SE) topology. Arrows in the images denote the placement of a single line on the USAF target which allows for comparison of the signals between detection schemes in (e-f). (e) Magnitude lines collected from each detection topology (color-coded) from the chrome-on-glass bars are compared. (f) Similarly, single phase lines from both topologies are compared between detection schemes. Theoretical phase delay from the 120 nm chrome-on-glass bars is denoted by the dashed black line. Scale bar, 0.2 mm.

much less noise present and more faithfully reconstructs the 120 nm chrome-on-glass bars in the phase image (Fig. 4f). These sample phase imaging results show potential for this scheme to allow for more accurate coherent detection in high speed or noisy applications. Also, the differential case provides less corrupted signals for input into calibration as well as input into phase unwrapping algorithms which are notoriously susceptible to noise.

In summary, we have introduced a design for a shot-noise limited coherent receiver which relies on the intrinsic phase-shifted output signals of 3x3 fused fiber couplers. Our topology utilizes balanced detectors to perform hardware-based subtraction that is necessary for projection of the signal's real and imaginary parts while also improving SNR and phase stability. This design extends previous work in 3x3 coherent receiver designs to include both calibration for more accurate results and balanced detection for decreased sensitivity to noise. We expect this fiber-based design to enable fast, reliable quadrature projection for numerous coherent detection applications.

Acknowledgments. Vortex OCT library functions written by Mark Draelos were crucial to development of real-time imaging control and acquisition code.

Disclosures. All authors are inventors on a provisional patent related to this work.

REFERENCES

1. E. Ip, A. P. T. Lau, D. J. F. Barros, and J. M. Kahn, Opt. Express **16**, 753 (2008).
2. G. Stoilov, and T. Dragostinov, Opt. Lasers Eng. **28**, 61 (1997).
3. Y.-Y. Cheng, and J. C. Wyant, Appl. Opt. **23**, 4539 (1984).
4. P. de Groot, and L. Deck, J. Mod. Opt. **42**, 389 (1995).
5. N. Brock, J. Hayes, B. Kimbrough, J. Millerd, M. North-Morris, M. Novak, and J. C. Wyant, Novel Optical Systems Design and Optimization VIII, (SPIE, 2005), 101.
6. M. Žurauskas, R. R. Iyer, and S. A. Boppart, Biomed. Opt. Express **12**, 981 (2021).
7. Y. Gong, J. Shi, D. Guang, M. Zhou, S. Mu, X. Wu, C. Zuo, and B. Yu, J. Light. Technol. **41**, 1357 (2023).
8. J. Hsieh, J. Pang, D. Yu, and Y. Sha, (Optoplex Corporation, 2009).
9. R. G. Priest, IEEE Trans. Microw. Theory Tech. **30**, 1589 (1982).
10. M. A. Choma, C. Yang, and J. A. Izatt, Opt. Lett. **28**, 2162 (2003).
11. C. Xie, P. J. Winzer, G. Raybon, A. H. Gnauck, B. Zhu, T. Geisler, and B. Edvold, Opt. Express **20**, 1164 (2012).
12. S. J. Savory, G. Gavioli, R. I. Killey, and P. Bayvel, Opt. Express **15**, 2120 (2007).
13. M. V. Sarunic, M. A. Choma, C. Yang, and J. A. Izatt, Opt. Express **13**, 957 (2005).
14. M. V. Sarunic, B. E. Applegate, and J. A. Izatt, Opt. Lett. **31**, 2426 (2006).
15. S. Park, S. Rim, Y. Kim, and B. H. Lee, Opt. Lett. **44**, 2590 (2019).
16. S. Park, J. Lee, Y. Kim, and B. H. Lee, Sensors **20**, 2665 (2020).
17. X. Attendu, D. J. Faber, G. Lamouche, T. G. v. Leeuwen, C. Boudoux, and M. Rivard, J. Biomed. Opt. **27**, 116006 (2022).
18. Y. Painchaud, M. Poulin, M. Morin, and M. Têtu, Opt. Express **17**, 3659 (2009).
19. Y. Mao, S. Sherif, C. Flueraru, and S. Chang, Appl. Opt. **47**, 2004 (2008).
20. X. Zhang, Z. Li, J. Li, C. Yu, A. P. Lau, and C. Lu, Opt. Lett. **39**, 5248 (2014).
21. A. M. Rollins, and J. A. Izatt, Opt. Lett. **24**, 1484 (1999).
22. M. A. Choma, A. K. Ellerbee, C. Yang, T. L. Creazzo, and J. A. Izatt, Opt. Lett. **30**, 1162 (2005).
23. M. Draelos, Vortex - an open-source library for building real-time oct engines in C++ or Python, https://www.vortex-oct.dev/, 2022.

REFERENCES

1. E. Ip, A. P. T. Lau, D. J. F. Barros, and J. M. Kahn, "Coherent detection in optical fiber systems," Opt. Express **16**, 753-791 (2008).
2. G. Stoilov and T. Dragostinov, "Phase-stepping interferometry: five-frame algorithm with an arbitrary step," Opt. Lasers Eng. **28**, 61-69 (1997).
3. Y.-Y. Cheng and J. C. Wyant, "Two-wavelength phase shifting interferometry," Appl. Opt. **23**, 4539-4543 (1984).
4. P. de Groot and L. Deck, "Surface Profiling by Analysis of White-light Interferograms in the Spatial Frequency Domain," J. Mod. Opt. **42**, 389-401 (1995).
5. N. Brock, J. Hayes, B. Kimbrough, J. Millerd, M. North-Morris, M. Novak, and J. C. Wyant, "Dynamic interferometry," in *Novel Optical Systems Design and Optimization VIII*, (SPIE, 2005), 101-110.
6. M. Žurauskas, R. R. Iyer, and S. A. Boppart, "Simultaneous 4-phase-shifted full-field optical coherence microscopy," Biomed. Opt. Express **12**, 981-992 (2021).
7. Y. Gong, J. Shi, D. Guang, M. Zhou, S. Mu, X. Wu, C. Zuo, and B. Yu, "Improved Algorithm for Phase Generation Carrier to Eliminate the Influence of Modulation Depth With Multi-Harmonics Frequency Mixing," J. Light. Technol. **41**, 1357-1363 (2023).
8. J. Hsieh, J. Pang, D. Yu, and Y. Sha, "Optical Hybrid Enables Next-Generation Optical Communication," (Optoplex Corporation, 2009).
9. R. G. Priest, "Analysis of Fiber Interferometer Utilizing 3 x 3 Fiber Coupler," IEEE Trans. Microw. Theory Tech. **30**, 1589-1591 (1982).
10. M. A. Choma, C. Yang, and J. A. Izatt, "Instantaneous quadrature low-coherence interferometry with 3× 3 fiber-optic couplers," Opt. Lett. **28**, 2162-2164 (2003).
11. C. Xie, P. J. Winzer, G. Raybon, A. H. Gnauck, B. Zhu, T. Geisler, and B. Edvold, "Colorless coherent receiver using 3x3 coupler hybrids and single-ended detection," Opt. Express **20**, 1164-1171 (2012).
12. S. J. Savory, G. Gavioli, R. I. Killey, and P. Bayvel, "Electronic compensation of chromatic dispersion using a digital coherent receiver," Opt. Express **15**, 2120-2126 (2007).
13. M. V. Sarunic, M. A. Choma, C. Yang, and J. A. Izatt, "Instantaneous complex conjugate resolved spectral domain and swept-source OCT using 3× 3 fiber couplers," Opt. Express **13**, 957-967 (2005).
14. M. V. Sarunic, B. E. Applegate, and J. A. Izatt, "Real-time quadrature projection complex conjugate resolved Fourier domain optical coherence tomography," Opt. Lett. **31**, 2426-2428 (2006).
15. S. Park, S. Rim, Y. Kim, and B. H. Lee, "Noncontact photoacoustic imaging based on optical quadrature detection with a multiport interferometer," Opt. Lett. **44**, 2590-2593 (2019).
16. S. Park, J. Lee, Y. Kim, and B. H. Lee, "Nanometer-scale vibration measurement using an optical quadrature interferometer based on 3× 3 fiber-optic coupler," Sensors **20**, 2665 (2020).
17. X. Attendu, D. J. Faber, G. Lamouche, T. G. v. Leeuwen, C. Boudoux, and M. Rivard, "Calibration procedure for enhanced mirror artifact removal in full-range optical coherence tomography using passive quadrature demultiplexing," J. Biomed. Opt. **27**, 116006 (2022).
18. Y. Painchaud, M. Poulin, M. Morin, and M. Têtu, "Performance of balanced detection in a coherent receiver," Opt. Express **17**, 3659-3672 (2009).
19. Y. Mao, S. Sherif, C. Flueraru, and S. Chang, "3× 3 Mach-Zehnder interferometer with unbalanced differential detection for full-range swept-source optical coherence tomography," Appl. Opt. **47**, 2004-2010 (2008).
20. X. Zhang, Z. Li, J. Li, C. Yu, A. P. Lau, and C. Lu, "Low-cost coherent receiver for long-reach optical access network using single-ended detection," Opt. Lett. **39**, 5248-5250 (2014).
21. A. M. Rollins and J. A. Izatt, "Optimal interferometer designs for optical coherence tomography," Opt. Lett. **24**, 1484-1486 (1999).
22. M. A. Choma, A. K. Ellerbee, C. Yang, T. L. Creazzo, and J. A. Izatt, "Spectral-domain phase microscopy," Opt. Lett. **30**, 1162-1164 (2005).
23. M. Draelos, Vortex - An open-source library for building real-time OCT engines in C++ or Python, https://www.vortex-oct.dev/, 2022.